Tracing the Active Phase and Dynamics for Carbon Nanofiber Growth on Nickel Catalyst Using Environmental Transmission Electron Microscopy

Yiqiang Lyu, Peng Wang, Dongdong Liu, Fan Zhang, Thomas P. Senftle,*
Guanghui Zhang, Zhenyu Zhang,* Jianmei Wang, and Wei Liu*

Benefitting from outstanding ability of C—C reforming and hydrogen activation, nickel is widely applied for heterogeneous catalysis or producing high-quality carbon structures. This high activity simultaneously induces uncontrollable carbon formation, known as coking. However, the activity origin for growing carbon species remains in debate between the on metallic facets induction and nickel carbide segregation. Herein, carbon growth on Ni catalyst is tracked via in situ microscopy methods. Evidence derived from high-resolution transmission electron microscopy imaging, diffraction, and energy loss spectroscopy unambiguously identifies Ni_3C as the active phase, as opposed to metallic Ni nickel or surface carbides as traditionally believed. Specifically, Ni_3C particle grows carbon nanofibers (CNF) layer-by-layer through synchronized oscillation of tip stretch and atomic step fluctuations. There is an anisotropic stress distribution in Ni_3C that provides the lifting force during nanofiber growth. Density functional theory computations show that it is thermodynamically favorable for Ni_3C to decompose into Ni and surface-adsorbed carbon. Carbonaceous deposits aggregate asymmetrically round the particle because partial surface is exposed to the hydrocarbon environment whereas the bottom side is shielded by the support. This induces a carbon concentration gradient within the particle, which drives C migration through Ni_3C phase before it exits as CNF growth.

1. Introduction

Controllable synthesis of carbon materials, e.g., nanotubes (CNTs) and graphene, with desired structures attracts much attention owned to remarkable physical and chemical properties.[1] As for both scientific and industrial interests, Ni-catalyzed chemical vapor deposition (CVD) is the widely used for its high yields and low cost.[2] Whereas, fabricating carbon materials with well-defined structure, e.g., specific stacking layers and helical angle, is still challenging due to the insufficient knowledge on dynamics control of carbon growth.[3] On the other hand, in catalysis reactions where nickel is involved, the outstanding ability of C—C reforming and hydrogen activation ensures ideal catalytic performance of cracking and hydrogenation, but simultaneously suffering from coking due to uncontrollable carbon formation.[4] Numerous solutions have been applied to restrain the unwanted carbon growth but bring limited efficiency.[5] Therefore, from perspectives of either facilitating catalytic reaction of long-term stability with minimized coking, or fabricating carbon materials of specific layers and stacking architecture, it is of high importance to control the migration and coupling processes of carbon atoms in Ni catalyst based on well understanding about reaction dynamics.[6]

Although Ni-catalyzed carbon growth has been studied in previous research, detailed knowledge is still ambiguous,

Y. Q. Lyu, D. D. Liu, Z. Z. Zhang
Key Laboratory for Precision and Non-Traditional Machining Technology
of Ministry of Education
Dalian University of Technology
2 Linggong Road, Dalian 116024, China
E-mail: zzy@dlut.edu.cn
Y. Q. Lyu, D. D. Liu, F. Zhang, W. Liu
Division of Energy Research Resources
Dalian Institute of Chemical Physics
Chinese Academy of Sciences
457 Zhongshan Road, Dalian, Liaoning 116023, China
E-mail: weiliu@dicp.ac.cn

P. Wang, T. P. Senftle
Department of Chemical and Biomolecular Engineering
Rice University
Houston, TX 77005, USA
E-mail: tsenftle@rice.edu
F. Zhang, W. Liu
University of Chinese Academy of Sciences
Beijing 100049, China
G. H. Zhang
State Key Laboratory of Fine Chemicals
PSU-DUT Joint Center for Energy Re-search
School of Chemical Engineering
Dalian University of Technology
Dalian 116024, China
J. Wang
School of Mechanical Engineering
Taiyuan University of Science and Technology
Taiyuan 030024, China

including the active phase and growth dynamics. Regarding on the active phase, early microscopy studies suggested that the catalysts stay as the metallic nickel according to in situ imaging results,[7] whereas theoretical calculation,[8] in situ XRD[9] and in situ XPS[10] coincidentally reported the existence of the intermedia carbide. Lack of direct evidence, particularly the absence of structure-resolved microscopy ones leaves this debate long-standing for decades. Most recently, by using in situ transmission electron microscopy (TEM) study, Huang X., Zhang L. and their co-workers found Co_3C and Fe_3C to be the active phase for respective carbon growth,[11] which inspires reconsideration of activity origin for nickel. Yu et al. report chemically synthesized Ni_3C could decompose giving rise to carbon formation.[12] This reversible conversion between metallic Ni and its carbides indicates the metastable Ni_xC could be a possible source to produce carbon spices. In this assumption, nickel carbide is unstable and tends to decompose out of reaction, this would leave Ni metals to be observed by ex situ or static characterizations. So only by in situ tracking the evolution of Ni catalyst during carbon formation, can the real active phase be identified.

Besides the efforts to reveal active phase, carbon growth dynamics catalyzed by Ni are also unclarified. On one hand, to the general experience, Ni(111) facets are considered to be essential for it has best fit with the graphene lattices to accommodate an epitaxial growth.[13] Given catalyzed by a Ni particle, graphite layers normally include a typical angle of 70° or 110° as determined by the geometry of adjacent Ni(111) facets.[14] Whereas according to other reports of in situ technology and theoretical calculation,[15] step sites are found as the starting point for initiating carbon growth ascribe to the low coordination at these sites for bonding adsorbates. It remains to be clarified about the role of Ni(111) facets and step sites. In addition, as frequently reported that Ni particle endures an oscillating reconstruction when catalyzing the CNT growth, the dynamics hiding behind remains unclear, such as reconstruction kinetics at Ni-graphene interface, the driving force for carbon atoms migration et al.

In this work, we perform systematic electron microscopy investigations to explore the activity origin of Ni-catalyzed carbon growth. The atomic structures and stress distribution at Ni/carbon interface was disclosed using spherical aberration correction scanning transmission electron microscopy (AC-STEM). The continuous carbon growth and fluctuated Ni reconstruction were traced in real time by utilizing ETEM combined with gas-cell technology. In the combination of theoretical simulation results, our discovery sheds light on the dynamic details of carbon growth process and serves as reference for controlled carbon synthesis.

2. Results

2.1. Epitaxial Growth of Ni@graphite and Interface Structure

Since the gas-solid reaction has been maturely adapted for producing carbons under transition metal catalysis,[7,11a] we tried solid-solid reaction scheme using graphene as solid carbon source to explore distinctive growth manners of carbon spices, it turned out to yield typical CNF (carbon nanofiber) struc-

ture in "herringbone" shape[16] similar to the results of those gas–solid works. As shown in **Figure 1**, in the Ni-catalyzed CNF structure, Ni particle is partially enclosed by multiwalled graphite after reaction at 450 °C for 1 h. It is worth noting that the Ni particles are in a homogenous morphology of wedge-shaped polyhedrons with elongated tips (Figure 1a), where the as-formed graphite layers are in tiled encapsulation parallel to particle facets (Figure 1b,c). It measures to be a fixed angle of either 110° or 70°, which coincides with the crystallography angle of two adjacent Ni(111) facets. This further implies epitaxial growth characteristic at the Ni-C interface that agrees with traditional knowledge.[17–19] Through STEM-BF observation (Figure 1c), there are quite few carbon layer on the non-Ni(111) facets due to the mismatch of the lattice symmetry. Specifically, a (200) facet is bridged over by bending graphite layers grown from two neighboring Ni(111) facets. Moreover, symmetry broken at local sites of Ni(111) that containing serrated edges and stacking faults (Figure 1g) would induce failure of graphite formation (Figure 1c marked by red arrow). In addition, there coexist two different stacking configuration of graphite layers over Ni(111), termed as "fcc" for face centered cubic and "hcp" for hexagonal close pack. As verified in combination of STEM imaging and microscopy simulations, the atomic structures at the Ni(111)/graphite interface have been disclosed. On the top side interface, the carbon atoms with the angle of 120° are located above the first layer of Ni atoms and the other three C atoms lay at the fcc hollow sites (Figure 1e). While for left side interface covered with hcp-stacking graphene (Figure 1f) three C atoms atop Ni sites and other ones stay at the hcp hollow sites. According to recent study, the different interfacial configurations could be attributed to the discrepant concentrations of subsurface interstitial carbon inside Ni crystal.[20] It therefore indicates that the surface symmetry of Ni atoms as well as subsurface carbon concentration play critical roles for inducing the formation of graphene layer. Besides the investigation on Ni/Graphene epitaxial interface, we studied the stress distribution using a geometry phase analysis (GPA) method to explore CNF growth mechanism. As demonstrated in Figure 1h,i, the varied interplanar spacing present inside the Ni crystal is in a anisotropic distribution. It is quite interesting to find that there is no obvious strain to the direction of Ni(111)/Graphite interface (exx') (Figure 1h), whereas a compression stress dominantly distributes along direction (eyy') perpendicular to the epitaxial interface, which is exactly the CNF growth direction (Figure 1i). Specially, this delicate strained Ni@graphite nanostructure is expected to derive as efficient nickel catalyst for the oxidation resistant provided by the graphite shell.[21]

However, for carbon growth there is still no evidence showing this metallic Ni as active phase, in situ microscopy study is highly necessary.

2.2. In Situ Tracing Carbon Growth and Ni Active Phase

The in situ experiment was further performed to trace the dynamic behaviors of Ni catalyst during carbon formation, which is essential to unravel the possible intermedia phase of catalytically active. Diffraction pattern of a large area of sample proves the metallic status of Ni particles after in situ
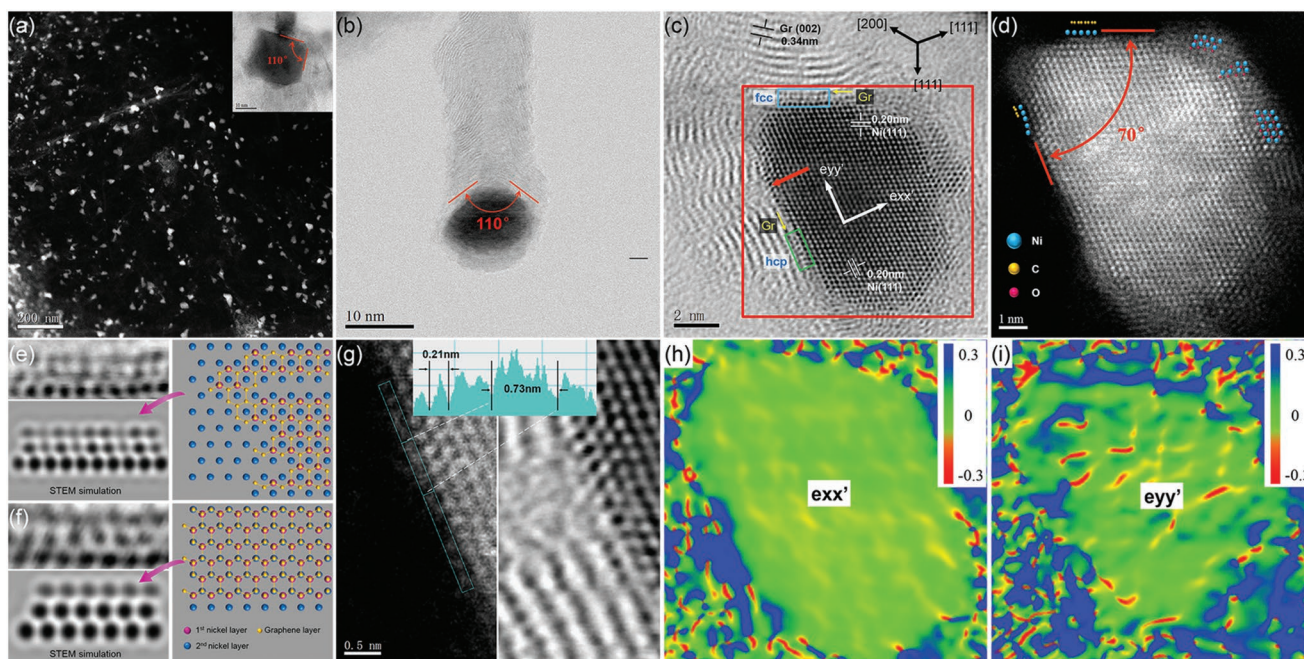
**ADVANCED
SCIENCE NEWS**
www.advancedsciencenews.com

**small
methods**
www.small-methods.com

Figure 1. Static observation of Ni/Graphite structure a) Dark-filed low-magnified TEM image of Ni/carbon composites. The inset shows one wedged Ni catalyst with carbon covering its (111) facets; b) TEM image of an individual CNF enclosing a catalyst particle in its head; c) STEM-BF image and d) STEM-HAADF image showing atomic structure of Ni@Graphite yielded after reaction; e) and f) are the enlarged STEM-BF images and their relative simulated ones from regions in Figure 1c marked with green and blue rectangles, respectively, structure models for STEM image simulation are in top view of the two Ni(111)/Graphene interfaces; g) enlarged DF and BF STEM images of stacking faults on the Ni (111) facet from region marked by red arrow in Figure 1c; h) and i) are the strain mapping for the red squared area in Figure 1c measured along G factors of the exx' $(111)_G$ and eyy' $(112)_G$, respectively.

pre-reduction (Figure S1a,b, Supporting Information). As the reaction gas (mixture of H_2 and CH_4) was introduced, the carbon structures growth initiated. The resulted carbon species are in typical morphology of multi-walled CNF, identical with reported situation of reforming reactions.[22] As demonstrated in Figure S2 (Supporting Information), **Figure 2** and Figure S1c,d (Supporting Information) the Ni-catalyzed carbon products generally falls into two typical characteristic morphologies, depending on reaction atmosphere (the H_2/CH_4 ratio). We denote one typical reaction scenario as "graphite mode," where carbon growth is not sustainable but stops at forming a graphite shell of several layers outside Ni particles (Figures S2a and S3a,l, and Movie S1 and S2, Supporting Information). The other configuration depicts as "CNF mode" that facilitating a continuous growth into elongated CNF structure (Figure S2b,c, Figure 2d–f and Movie S3, Supporting Information), which is in the same architecture as that in static TEM observation (Figure 1). Specifically, for the graphite mode, the graphite layers are not necessarily tiled on the Ni(111) facets, but some layers are in connection with surface steps of Ni through sharing their laterally exposed edges (Figure S4, Supporting Information). This indicates such step sites could be a source for carbon atoms separation to form graphene layers. Besides, in graphite mode a reaction proceeds in a very short duration before coming to the stop when most catalyst particles decompose to be "dead" as nickel (Figure S3a–l, Supporting Information). As an exception, one individual particle was discovered to be in Ni_3C phase thanks to the protection by the NiO surface

(Figure 2a–c). It suggests this carbide phase could be active during reaction but readily degrades to nickel. This deduction is further supported when the same phase transition has been found in the CNF mode (Figure 2d–f and Movie S3, Supporting Information). The CNF structure was grown as catalyzed by Ni_3C particle, which reversely turned back to nickel as reaction stopped (Figures S3, S4, and S5b, Supporting Information).

Since the Ni_3C shares the same stacking of Ni atoms with hcp-Ni phase and in situ movement of Ni particles blurs spatial resolution of TEM data. Therefore, to achieve more solid evidence about Ni_3C intermedia, in situ electron energy loss spectroscopy (EELS) as well as in situ diffraction methods have been utilized. In this strategy, the promoted reaction efficiency owned to high pressure gas-cell technology ensures majority of particles to stay active to simultaneously catalyze the carbon growth. It therefore facilitates reliable detection on this active phase analyzed by the overall analysis of in situ EELS and selected area electron diffraction (SAED). Results show that the as-formed CNF structure is in typical graphitic status with both π^* and σ^* features for C-K edge (Figure S5, Supporting Information).[23] Further optimizing the point analysis operation via predicting the moving path of one working catalyst particle, we were able to capture EELS signals of the active phase as shown in Figure 2g–i. The particle site contains carbon species whose EELS spectrum shows distinctive features (red line in Figure 2h) not like to the reference spectrum from CNF (blue line Figure 2h), which implies such carbon species locate inside the particle rather than graphite shell encapsulating outside.
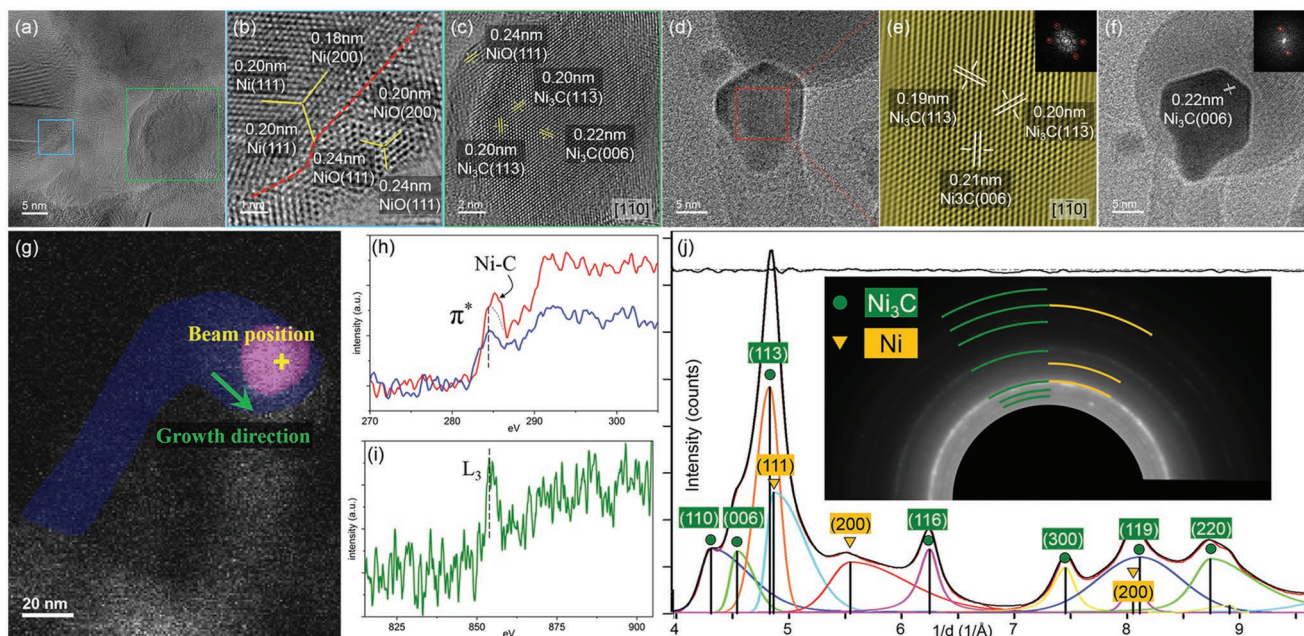
Figure 2. Phase reconstruction of Ni catalyst during carbon growth. a) HRTEM image of a particle after reaction. b,c) The magnified atom-resolved images from highlighted regions in (a) with blue and green squares, respectively. d–f) TEM images of one active particle during the reaction in the CNF mode. (e) is the Fourier-filtered HRTEM of the red square area in (d). g) Illustration on an in situ EELS analysis via tracing a migrating Ni particle during reaction. h,i) EELS spectra (raw data) of C-L edge (red) and Ni-L edge collected from Ni particle as marked in (g), blue lined spectrum in (h) is a reference collected from the CNF near Ni particle in (g). j) The integrated intensity profile for phase index and the inset is the in situ SAED pattern, profile upsides in (j) is the residual error of deconvolutional fitting of the diffraction profile.

Specially, the carbon spectrum shows a remarkably higher and wider K edge, which in deconvolution of $\pi*$ signal (≈284 eV) of graphite and the strong peak at ≈286 eV. This distinct peak at higher loss energy can be attributed to Ni-C $\sigma*$ bond of nickel carbide,[10,24] because carbon in Ni_xC has no $\pi*$ bond and the bonding with nickel lowers the $\sigma*$ orbit thus yielding higher loss energy. Such Ni_xC phase has been furthers identified to be Ni_3C in situ SAED evidence (Figure 2j, Movie S4, Supporting Information). In this analysis, radically integrated profile reflects diffraction characteristics of phase composition over a large number of catalyst particles. As the reaction started, catalysts of pure nickel status (Figure S6a, Supporting Information) initiate a progressive phase transformation toward Ni_3C within several seconds (Figure S6c–f, Supporting Information). It is worth noting that in all these in situ experiments some catalysts that do not succeed in carbon growth due to unsatisfied local condition stay as metallic Ni throughout the process (Figures S6 and S7, Supporting Information).

2.3. Carbon Growth Dynamics of Oscillating Reconstruction

As active Ni_3C has been evidenced, it encourages us to explore the growth dynamics of catalyzed carbon growth through the careful examination and quantification over in situ microscopy results. Noting that two carbon growth modes produce similar graphite layers but differ in stacking geometry, the vigorous CNF mode was focused herein to explore the reaction dynamics. In a typical growth process, the Ni_3C particle demonstrates oscillation characteristics consist of reconstruction

manners of three types, including the overall lifting as CNF grows, the periodic stretch and retraction of tip, and steepening on lateral facets (Movie S3, Supporting Information). First starting from 2.2s, atomic step emerges driven by spontaneously steepening at two neighboring facets (**Figure 3**a,b). Then the particle was stretched by 22% longer within 7 s along opposite direction of CNF growth (Figure 3c,d) when a tip is yielded and tiled on its surface with the newly formed graphene layers. Specially during this procedure, the tip keeps being stretched longer but stays unrotated overall as inducing carbon layers to stack backward to drive the growth CNF. This phenomenon suggests strong interactions exist at the Ni_3C/graphene interface. As the tip keeps being stretched, the shear stress increases to be strong enough to override the Ni-graphene interaction leading to the instant retraction (Figure 3e–h;); meanwhile the particle moves forward leaving an interspace between the tip and graphene layer (Figure 3f,h). Finishing the above behaviors, a dynamic catalytic cycle is completed before the next one starts from surface steepening (Figure 3i–l). It is worth noting that the step emerges and disappears in synchronization with the tip stretching and retracting. Every time a steepening occurs, the graphene layers are grown and vice versa. The synergized reconstructions facilitate the apparent CNF growth via alternative actions of graphene formation and Ni_3C particle movement.

2.4. Ab Initio Thermodynamics of Phase Formation

The relative stability of Ni_xC_y phases was assessed with ab initio thermodynamics to understand the state of the catalyst surface
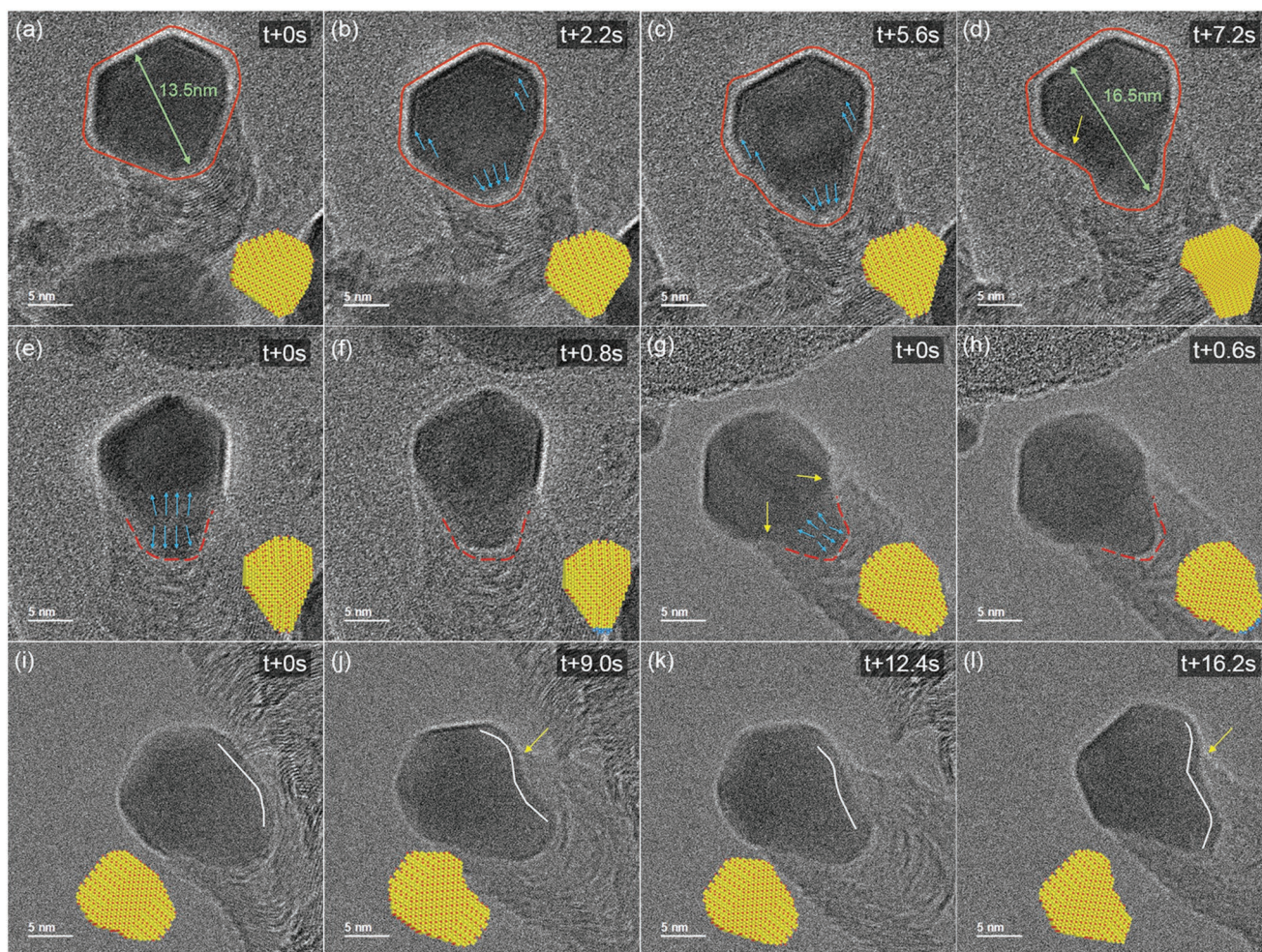
Figure 3. Sequential reconstructed stages of Ni$_3$C particle going through dynamic cycles of CNF growth. a–d) The elongation process of the catalyst. e–h) The periodically stretch and retraction of catalyst tip. i–l) the periodically steepening and flattening of step edges. The TEM image series are selected from continuously recorded process shown in Movie S3 (Supporting Information). The orange lines, the white lines and the red dash lines depicts the outline of the catalyst, periodically changing surface and the position of the catalyst tip, respectively. The blue and yellow arrows indicate the inner stress and position of step sites, respectively.

under reaction conditions.[7a] The computed phase diagram of bulk Ni$_x$C$_y$ is shown in **Figure 4**a, which shows that Ni$_3$C is less stable than separate Ni and graphite phases, which suggests that Ni$_3$C is a metastable phase that would spontaneously decompose from the standpoint of thermodynamic stability. Indeed, our in situ experiments show that catalyst particles of Ni$_3$C eventually end up generating graphite and deactivating. To obtain a Ni$_3$C phase, the system has to be forced into a non-equilibrium steady-state wherein carbon atoms deposited from the gas phase are continuously removed from the surface so that the accumulation of carbon atoms is prevented and graphite is not able to form which allows Ni$_3$C to be the most stable phase. The decomposition of Ni$_3$C into bulk Ni and surface-adsorbed carbon layers was further investigated by calculating the surface formation energy of Ni$_3$C surfaces compared to graphene adsorbed on a pure Ni surface. These surface models are shown in Figure S12 (Supporting Information). The surface free energies of two terminations of the Ni$_3$C(001) facet (a carbon-terminated surface and a Ni-terminated surface)

and of a graphene layer adsorbed on Ni(111) are shown in Figure 4b. The energy of bulk Ni$_3$C is taken as the reference for the Ni atoms. The terminations of Ni$_3$C(001) are either Ni-rich or C-rich (i.e., their stoichiometry is different from that of bulk Ni$_3$C) so their relative surface free energies depend on the chemical potential of carbon. The ratio of Ni to C atoms in the graphene-on-Ni(111) model is 3:1, so its surface free energy, which was defined relative to stoichiometric Ni$_3$C, is constant on this graph. The surface free energy of graphene-on-Ni(111) is much lower than that of the Ni$_3$C(001) surfaces. Thus, there is a strong thermodynamic driving force for Ni$_3$C surfaces to decompose into metallic Ni and graphene.

As demonstrated in Figure 4, there is a strong driving force for Ni$_3$C to decompose into metallic Ni and graphene. With this insight, we propose a structural evolution process as shown in **Figure 5**. Initially, the phase transition from Ni to Ni$_3$C occurs since Ni$_3$C is the stable phase when graphite is not yet formed. On the upper half of the catalyst particle, atomic carbon will accumulate on the Ni$_3$C surfaces from hydrocarbon deposition,
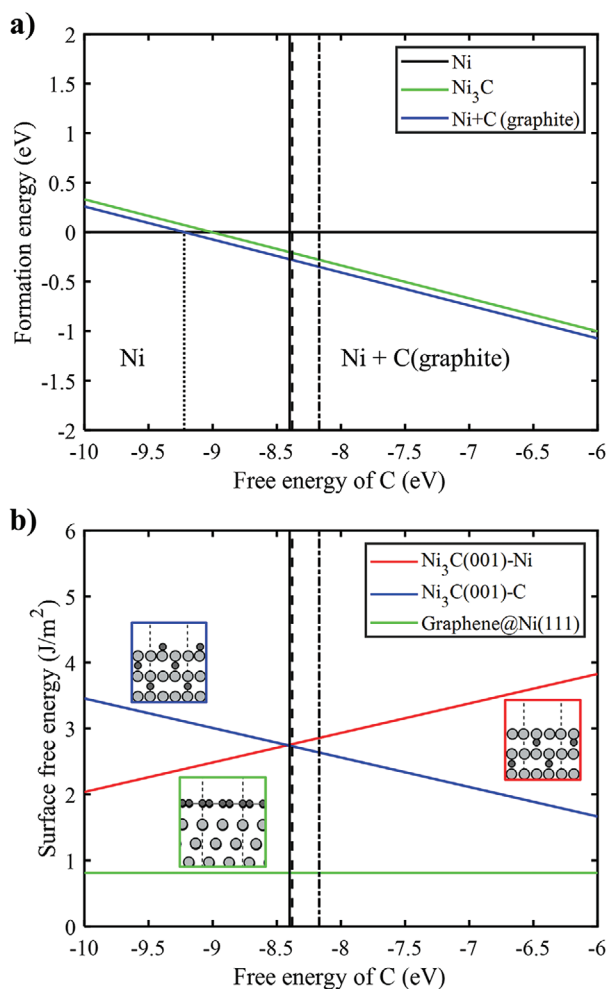
**ADVANCED
SCIENCE NEWS**

www.advancedsciencenews.com

**small
methods**

www.small-methods.com

Figure 4. Phase diagram of energy preference over Ni₃C/Ni-Carbon system. a) The phase diagram of bulk phases. The *x*-axis is the free energy of C which is referenced to the gas phase species. The *y*-axis is the formation energy of each bulk phase relative to Ni(fcc). The black line is Ni(fcc), the green is Ni_3C, and the blue is bulk Ni(fcc) + bulk C(graphite) in which the Ni:C ratio is 3:1. The colored dotted long vertical lines are the locations of the following reaction conditions at 773.15 K: green solid line (2.16×10^{-3} atm CH_4, 5.4×10^{-4} atm H_2), red dashed line (1.8×10^{-3} atm CH_4, 9×10^{-4} atm H_2), and blue dash-dotted line (2.5×10^{-1} atm C_2H_2, 2.5×10^{-1} atm H_2). b) The *y*-axis is the free energies of surface structures computed relative to bulk Ni_3C. The red line is the Ni-rich termination of $Ni_3C(001)$, the blue line is the C-rich termination of $Ni_3C(001)$, and the green line represents a graphene layer adsorbed on Ni(111), where the surface model has a Ni:C ratio of 3:1. The side views of each surface model are shown with insets, where the color of border matches corresponding colored line. Carbon atoms are black, Nickel atoms are gray.

and this carbon will migrate into the crystal and form a domain of carbon accretion. The lower half of the particle is contacted with the support and, as such, hydrocarbons are not able to reach the surface of the particle, thus establishing a concentration gradient of carbon across the particle. Carbon atoms migrate against the concentration gradient and egress from the surface as graphene layers, which is illustrated in Figure 4b. The escaped carbon from the subsurface maintains the carbon concentration gradient and carbon diffusion from the top domain to the bottom domain, as shown in Figure 5. Balancing

the rate of carbon diffusion, which is determined by the concentration gradient, is key for achieving CNF growth. If the carbon diffusion process is not fast, carbon will escape from the top half of the particle and the Ni_3C phase will decompose to Ni and graphite. A flux of carbon can be maintained through the catalyst particle if diffusion is fast, which in turn yields a meta-stable Ni_3C phase that promotes CNF growth. These processes will be only observable with in situ characterizations since the Ni_3C phase and CNF growth need the specific gas phase environment to be maintained and they will decompose into Ni and graphite in carbon-poor *ex-situ* environments. This proposed CNF growth model on Ni_3C is similar in principle to the CNF growth on Fe_3C proposed in previous literature.[25]

3. Discussion

Despite similar dynamics of carbon growth, which Ni_3C shares with that of iron carbides and cobalt carbides, the mechanism of which has been well-understood in previous works.[11] However, the fundamental insights remain in unclarified for Ni catalysts, although applications have been extensively focused for decades. The critical reason lying behind is the strong degradation character of Ni_3C phase that presents it from being detected outside the reaction, whereas the carbide phase remains stable for Fe_3C and Co_3C. Even though microscopy study was realized in early period, Ni_3C was still missed from being identified, because some works were under ex situ condition when Ni_3C inevitably decomposes into Ni metal, while other in situ observations also failed to obtain clear-enough lattice information due to fast target movement and limited in situ resolution. On this basis in our work, the combination of in situ EELS and SAED is significantly necessary to fully confirm Ni_3C as well as exclude possible hcp-Ni. All the microscopy evidence suggests Ni_3C drives vigorous carbon formation ending with a universal Ni@graphite architecture, regardless of reaction environments and growth modes it went through (Figures S5b, S8, and S9, Supporting Information). This reaction is intrinsically facilitated in the dynamic equilibrium of sequential procedures involving CH_4/C_2H_2 decomposition and carburization, gradient carbon transportation, and crystal-geometry induced surface segregation.

Realizing quantitative analysis on behaviors of Ni particle, we were able to go deeper into above equilibrium. Through tracking the propagation of Ni/Graphene interface, the carbon growth rates has been obtained as shown Figure S10 (Supporting Information). For both modes, the graphite grows at specific rate differing among particles, but exclusively shows segmented increase of thickness (≈3.4Å) corresponding to a layer-by-layer growth behavior. In CNF mode, it grows faster at ≈2 nm s⁻¹ (Figure S10a, Supporting Information), close to the speed reported before.[26] Comparatively in graphite mode, it proceeds at much slower rate of 0.12 nm s⁻¹ and the growth cycle is extended to 20 s (Figure S10b, Supporting Information). The difference in carbon growth rate is due to the difference status of Ni particles. In CNF mode carbon atoms segregate fast out of Ni_3C driven by the high transportation dynamics of carbon spices. Whereas for graphite mode, such transportation equilibrium is interrupted due to gradual coverage of
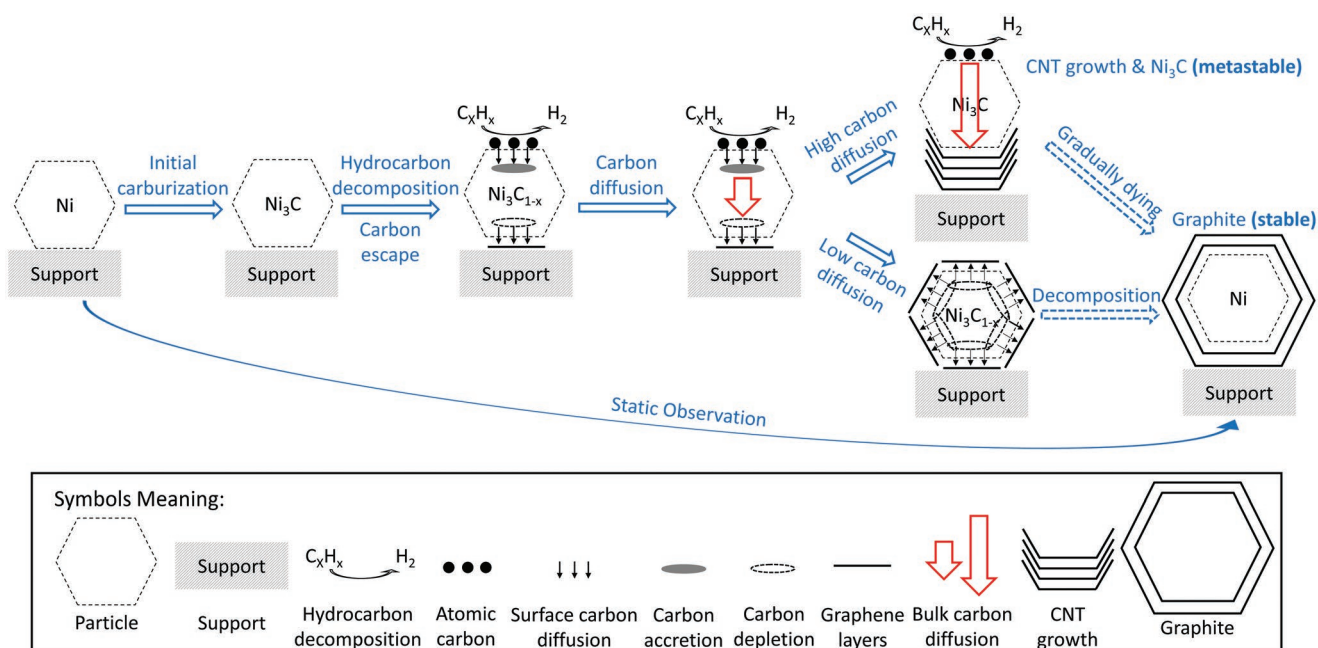
ADVANCED
SCIENCE NEWS
www.advancedsciencenews.com

small
methods
www.small-methods.com

Figure 5. Scheme of different catalyst-development paths that are determined by the hydrocarbon decomposition rate.

graphite layers blocking carburization supplement, therefore the depletion of carbon concentration inside Ni_xC slowers down the growth rate. It is worthwhile to specify that growth rate is inversely proportional to growth duration and corelates with the particle size. Given bigger particle in graphite mode (Figure S3d, Supporting Information), it presents higher growth rate and shorter growth duration that of smaller particle (Figure S10c, Supporting Information). This is because in such unstainable process the carbon capacity stored inside Ni_3C generally determines the growth behaviors. Moreover, there is a time interval when the carbon growth rate stays zero, this could be ascribed to the relaxation stage where particle reconstructs to and rebuilds the carbon gradient for initiating next growth cycle.

On the basis of microscopy evidence and discussions presented above, a roadmap is drawn as in Figure S11 (Supporting Information), which contains all possible reconstruction pathways for Ni catalyst. The evolution direction of a certain growth process would be intrinsically determined by dynamic equilibrium of sequential procedures involving CH_4/C_2H_2 decomposition and carburization, gradient formation carbon transportation inside Ni_3C, and carbon surface segregation induced by crystal-geometry.

4. Conclusion

In this work, we used in situ microscopy method and DFT simulations to identify the active phase and growth dynamics of nickel catalyst for carbon formation. Solid conclusions can be drawn that Ni_3C, not the previously proposed metal Ni, is the active phase during the reaction. This active phase also acts as the intermedia to facilitate carbon conversion from decomposition of methane/acetylene to CNF/graphite. The carbon growth

can endure two modes, "graphite mode" and "CNF mode" that are intrinsically determined by dynamic equilibrium of carbon transportation and segregation over Ni_3C. In both growth modes, the Ni_3C phase catalyzes the layer-by-layer growth of carbon products while going through synchronized reconstruction of tip stretch and atomic steps fluctuation. Furthermore, there is anisotropic stress distribution inside Ni_3C crystal that provides the lifting force during CNF growth. The asymmetrically distributed procedures of Ni carburization and carbon segregation over one catalyst particle induces a carbon concentration gradient to drive atoms migration inside Ni_3C. This work modifies previous understanding about the Ni-catalyzed carbon growth, clarifies the activity origin, and highlights the significance of in situ methods in studying a catalytic process.

5. Experimental Section

Ex Situ Carbon Reconstruction on Ni: As-prepared reduction graphene oxide (RGO, 25.0mg) synthesized by Hummer's method was added to the deionized water and stirred for 10 min, followed by one-hour ultrasonic vibration mixing. Then, $Ni(NO_3)_2 \cdot 6H_2O$ was added, followed by another hour of ultrasonic vibration. Freshly prepared $NaBH_4$ solution was added dropwise to gain the precursor. After being stirred for 2 h under room temperature and following annealing process, the products was collected through centrifugation. Repetitive scour in deionized water and ethanol is conducted prior to products' being proposed in drying oven (60 °C). In the end, the final target products were obtained through annealing treatment in tube furnace with 2% H_2 in Ar (450 °C)

Scanning Transmission Electron Microscopy Analysis: STEM analyses were carried out on a double-corrected JEOL 3100R5 (the prototype of JEM ARM300F) microscope with cold-field emission gun working under 300 kV. The sample was prepared via dissolving the powder into the ethanol under ultrasonic dispersion. A drop of the suspension was dispersed onto the copper grid. JEOL JEM 2100F microscope equipped with a CEOS GmbH probe corrector and was operated at 200 kV in

**ADVANCED
SCIENCE NEWS**

www.advancedsciencenews.com

**small
methods**

www.small-methods.com

STEM mode with a probe convergence angle of 28 mrad and the annular detection range of the annular dark- field detector was set to collect electrons scattered between 45 and 180 mrad for the HAADF images.

STEM Images Simulation: To address the configuration structure clearly, images simulation using the QSTEM software was performed for key areas. The following calculation parameters were applied in the simulation: acceleration voltage of 300 kV; object aperture (8 mrad); defocus (−8 nm); spherical aberration (1 μm). Possible structures were built and calculated to verify the hypothesis of atoms arrangements in real images.

Geometry Phase Analysis (GPA): Strain characterization was performed through GPA. The stress measurement is based on the displacement of atom columns along the diffraction vectors of exx' $(111)_G$ and eyy' $(112)_G$, respectively. The matrix from central region of Ni particle was used as the strain-free reference. If the interplanar space shrinks, it yields compression strain in proportional to the displacement, while it produces tensile strain appears in converse situation. Lattice fringe contrasts were colored according to the strain value, colors with positive values stands for compressive strains and those with negative values represent tensile strains. The value in the scale bar stands for the ratio of interplanar spacing variation to its original value. Positive value represents tensile and negative one means compression.

In Situ TEM Experiment: Nickel supported on silica-alumina (62%) was purchased from Alfa Aesar. The as-prepared sample was dispersed into ethanol under ultrasonic dispersion for 10 min. A drop of this solution was transferred onto the NanoEX heating chip for in situ ETEM study. The in situ experiment was performed in the FEI Titan Cubed Themis G3 300 with home-built gas supply system. During the in situ characterization, H_2 (2mabr) was first introduced followed by increasing the temperature to 600 °C to reduce possible NiO on particle surface. After reduction, the reaction gas environment was switched into a mixture of H_2 and CH_4 (total pressure 2.7 mbar) as the reaction temperature was raised to 500 °C at the rate of 5 °C s^{-1}. By increasing the ratio of CH_4 to H_2 from 2 to 4, the carbon growth efficiency can be promoted to switch the reaction from graphite mode to a continuous CNF mode. Besides, the electron dose rate keeps at very low level (<500 e Å^{-2} s^{-1}) when in situ recording the process of carbon growth. Similar phenomenon of carbon deposition was universally found in areas without beam irradiation, which proves less interference of beam effect on carbon growth process. Because in situ movement of Ni particles reduces TEM data quality, the error of lattice measurement for phase index is estimated to be within 5%.

In Situ EELS and SAED: The same sample from in situ TEM experiment was subject to in situ investigations of electron energy loss spectroscopy (EELS) and selected area diffraction (SAED). Ni catalyst was first dispersed onto the heating chip (DENs Solutions). The in situ experiment was performed in the FEI Titan Cubed Themis G3 300 with DENS Climate system. Specifically, the Ni catalyst was pre-reduced in H_2 (500 mbar) 500 °C for 30 min. Afterward, the temperature was lowered to 100 °C to switch the atmosphere into the reaction gas (C_2H_2:H_2 = 1:1, total pressure 500 mbar). Subsequently the temperature was raised to 500 °C at rate of 10 °C s^{-1} to initiate CNF growth. As catalytic reaction was carried on, EELS analysis was performed using GIF Quantum 965 system. At last, evolutionary SAED pattern were recorded using OneView camera at 4kx4k imaging resolution.

Density Functional Theory (DFT) Simulations: All DFT computations were performed with the Vienna ab initio simulation package (VASP 5.4.4).[27] The Perdew–Burke–Ernzerhof (PBE) functional was applied as the exchange-correlation functional.[28] Further computational settings are summarized in the Supporting Information.

Ab initio Thermodynamics: The formation energy of bulk structures containing varying amounts of Ni and C was computed with the following

$$\Delta E_{form} = E_{Ni_xC_y} - x \cdot E_{Ni(fcc)} - y \cdot \mu_C \tag{1}$$

where ΔE_{form} is the relative formation energy, $E_{Ni_xC_y}$ is the DFT energy of a bulk structure with x Ni atoms and y C atoms, $E_{Ni(fcc)}$ is the DFT energy

of metallic Ni(fcc) used as a uniform reference energy for Ni atoms, μ_C is the chemical potential of carbon derived from the free energy of gas species as a function of the operating conditions, as described in the Supporting Information.

The free energy of surface structures containing varying amounts of Ni and C were computed with the following

$$\gamma = \left[E_{Ni_xC_y} - x \cdot (E_{Ni_3C} - \mu_C)/3 - y \cdot \mu_C \right]/2A \tag{2}$$

where γ is the surface free energy, $E_{Ni_xC_y}$ is the DFT energy of a symmetric slab with x Ni atoms and y C atoms, E_{Ni_3C} is the DFT energy of bulk Ni$_3$C, μ_C is the chemical potential of carbon, and A is the surface area of the slab. The surface free energy respresents the energy required to form a surface from bulk Ni$_3$C under a carbon-rich environment.

Supporting Information

Supporting Information is available from the Wiley Online Library or from the author.

Acknowledgements

Conflict of Interest

The authors declare no conflict of interest.

Data Availability Statement

The data that support the findings of this study are available in the supplementary material of this article.

Keywords

[1] a) M. F. L. De Volder, S. H. Tawfick, R. H. Baughman, A. J. Hart, *Science* **2013**, *339*, 535; b) R. Rao, C. L. Pint, A. E. Islam, R. S. Weatherup, S. Hofmann, E. R. Meshot, F. Wu, C. Zhou, N. Dee, P. B. Amama, J. Carpena-Nunez, W. Shi, D. L. Plata, E. S. Penev, B. I. Yakobson, P. B. Balbuena, C. Bichara, D. N. Futaba, S. Noda,

H. Shin, K. S. Kim, B. Simard, F. Mirri, M. Pasquali, F. Fornasiero, E. I. Kauppinen, M. Arnold, B. A. Cola, P. Nikolaev, S. Arepalli, et al., *ACS Nano* **2018**, *12*, 11756.

[2] Q. Zhao, Z. Xu, Y. Hu, F. Ding, J. Zhang, *Sci. Adv.* **2016**, *2*, e1501729.

[3] S. Zhang, L. Kang, X. Wang, L. Tong, L. Yang, Z. Wang, K. Qi, S. Deng, Q. Li, X. Bai, F. Ding, J. Zhang, *Nature* **2017**, *543*, 234.

[4] a) S. Li, J. Gong, *Chem. Soc. Rev.* **2014**, *43*, 7245; b) M. Akri, S. Zhao, X. Li, K. Zang, A. F. Lee, M. A. Isaacs, W. Xi, Y. Gangarajula, J. Luo, Y. Ren, Y. T. Cui, L. Li, Y. Su, X. Pan, W. Wen, Y. Pan, K. Wilson, L. Li, B. Qiao, H. Ishii, Y. F. Liao, A. Wang, X. Wang, T. Zhang, *Nat. Commun.* **2019**, *10*, 5181.

[5] a) S. Shoji, X. Peng, T. Imai, P. S. Murphin Kumar, K. Higuchi, Y. Yamamoto, T. Tokunaga, S. Arai, S. Ueda, A. Hashimoto, N. Tsubaki, M. Miyauchi, T. Fujita, H. Abe, *Chem. Sci.* **2019**, *10*, 3701; b) S. Das, J. Ashok, Z. Bian, N. Dewangan, M. H. Wai, Y. Du, A. Borgna, K. Hidajat, S. Kawi, *Appl. Catal., B* **2018**, *230*, 220.

[6] D. Pakhare, J. Spivey, *Chem. Soc. Rev.* **2014**, *43*, 7813.

[7] a) S. Helveg, C. Lopez-Cartes, J. Sehested, P. L. Hansen, B. S. Clausen, J. R. Rostrup-Nielsen, F. Abild-Pedersen, J. K. Norskov, *Nature* **2004**, *427*, 426; b) S. Hofmann, R. Sharma, C. Ducati, G. Du, C. Mattevi, C. Cepek, M. Cantoro, S. Pisana, A. Parvez, F. Cervantes-Sodi, A. C. Ferrari, R. Dunin-Borkowski, S. Lizzit, L. Petaccia, A. Goldoni, J. Robertson, *Nano Lett.* **2007**, *7*, 602.

[8] a) M. G. Jiao, K. Li, W. Guan, Y. Wang, Z. J. Wu, A. Page, K. Morokuma, *Sci. Rep.* **2015**, *5*, 12091; b) M. G. Jiao, H. J. Qian, A. Page, K. Li, Y. Wang, Z. J. Wu, S. Irle, K. Morokuma, *J. Phys. Chem. C* **2014**, *118*, 11078.

[9] A. Rinaldi, J. P. Tessonnier, M. E. Schuster, R. Blume, F. Girgsdies, Q. Zhang, T. Jacob, S. B. A. Hamid, D. S. Su, R. Schlogl, *Angew. Chem., Int. Ed.* **2011**, *50*, 3313.

[10] A. Benayad, X. S. Li, *J. Phys. Chem. C* **2013**, *117*, 4727.

[11] a) X. Huang, R. Farra, R. Schlogl, M. G. Willinger, *Nano Lett.* **2019**, *19*, 5380; b) Y. Wang, L. Qiu, L. L. Zhang, D. M. Tang, R. X. Ma, Y. Z. Wang, B. S. Zhang, F. Ding, C. Liu, H. M. Cheng, *ACS Nano* **2020**, *14*, 16823.

[12] B. W. Yu, Q. K. Zhang, L. Z. Hou, S. L. Wang, M. Song, Y. H. He, H. Huang, J. Zou, *Carbon* **2016**, *96*, 904.

[13] A. Dahal, M. Batzill, *Nanoscale* **2014**, *6*, 2548.

[14] a) Q. K. Yu, J. Lian, S. Siriponglert, H. Li, Y. P. Chen, S. S. Pei, *Appl. Phys. Lett.* **2008**, *93*, 113103; b) L. Kepinski, B. Stasinska, T. Borowiecki, *Carbon* **2000**, *38*, 1845.

[15] a) S. Saadi, F. Abild-Pedersen, S. Helveg, J. Sehested, B. Hinnemann, C. C. Appel, J. K. Norskov, *J. Phys. Chem. C* **2010**, *114*, 11221; b) R. Rao, R. Sharma, F. Abild-Pedersen, J. K. Norskov, A. R. Harutyunyan, *Sci. Rep.* **2014**, *4*, 6510.

[16] R. T. K. Baker, in *Encyclopedia of Materials: Science and Technology* (Eds: K. H. J. Buschow, R. W. Cahn, M. C. Flemings, B. Ilschner, E. J. Kramer, S. Mahajan, P. Veyssière), Elsevier **2001**, pp. 932–941.

[17] L. Kępiński, B. Stasińska, T. Borowiecki, *Carbon* **2000**, *38*, 1845.

[18] R. Baker, *Carbon* **1989**, *27*, 315.

[19] K. S. Kim, Y. Zhao, H. Jang, S. Y. Lee, J. M. Kim, K. S. Kim, J.-H. Ahn, P. Kim, J.-Y. Choi, B. H. Hong, *Nature* **2009**, *457*, 706.

[20] S. C. Matysik, C. Papp, A. Gorling, *J. Phys. Chem. C* **2018**, *122*, 26105.

[21] L. Z. Bu, N. Zhang, S. J. Guo, X. Zhang, J. Li, J. L. Yao, T. Wu, G. Lu, J. Y. Ma, D. Su, X. Q. Huang, *Science* **2016**, *354*, 1410.

[22] S. Damyanova, B. Pawelec, K. Arishtirova, J. L. G. Fierro, *Int. J. Hydrogen Energy* **2012**, *37*, 15966.

[23] W. Q. Han, K. R. P. , T. Seeger, F. Ernst, M. Ruhle, N. Grobert, W. K. Hsu, B. H. Chang, Y. Q. Zhu, H. W. Kroto, D. Walton, M. Terrones, H. Terrones, *Appl. Phys. Lett.* **2000**, *77*, 1807.

[24] S. Grimme, J. Antony, S. Ehrlich, H. Krieg, *J. Chem. Phys.* **2010**, *132*, 154104.

[25] a) L. Zhou, L. R. Enakonda, M. Harb, Y. Saih, A. Aguilar-Tapia, S. Ould-Chikh, J. L. Hazemann, J. Li, N. Wei, D. Gary, P. Del-Gallo, J. M. Basset, *Appl. Catal., B* **2017**, *208*, 44; b) R. J. Wrobel, A. Helminiak, W. Arabczyk, U. Narkiewicz, *J. Phys. Chem. C* **2014**, *118*, 15434.

[26] R. Rao, R. Sharma, F. Abild-Pedersen, J. K. Norskov, A. R. Harutyunyan, *Sci. Rep.* **2014**, *4*, 6510.

[27] G. Kresse, J. Furthmuller, *Comput. Mater. Sci.* **1996**, *6*, 15.

[28] J. P. Perdew, K. Burke, M. Ernzerhof, *Phys. Rev. Lett.* **1996**, *77*, 3865.